Transient Increase in Arctic Deep-Water Formation and Ocean Circulation under Sea Ice Retreat

ANAÏS BRETONES,[a,b] KERIM H. NISANCIOGLU,[a,b,c] MARI F. JENSEN,[a,b] AILIN BRAKSTAD,[b,d] AND SHUTING YANG[e]

[a] *Department of Earth Science, University of Bergen, Bergen, Norway*
[b] *Bjerknes Centre for Climate Research, Bergen, Norway*
[c] *Centre for Earth Evolution and Dynamics, Department of Geosciences, University of Oslo, Oslo, Norway*
[d] *Geophysical Institute, University of Bergen, Bergen, Norway*
[e] *Danish Meteorological Institute, Copenhagen, Denmark*

(Manuscript received 23 February 2021, in final form 22 September 2021)

ABSTRACT: While a rapid sea ice retreat in the Arctic has become ubiquitous, the potential weakening of the Atlantic meridional overturning circulation (AMOC) in response to global warming is still under debate. As deep mixing occurs in the open ocean close to the sea ice edge, the strength and vertical extent of the AMOC is likely to respond to ongoing and future sea ice retreat. Here, we investigate the link between changes in Arctic sea ice cover and AMOC strength in a long simulation with the EC-Earth–Parallel Ice Sheet Model (PISM) climate model under the emission scenario RCP8.5. The extended duration of the experiment (years 1850–2300) captures the disappearance of summer sea ice in 2060 and the removal of winter sea ice in 2165. By introducing a new metric, the Arctic meridional overturning circulation (ArMOC), we document changes beyond the Greenland–Scotland ridge and into the central Arctic. We find an ArMOC strengthening as the areas of deep mixing move north, following the retreating winter sea ice edge into the Nansen Basin. At the same time, mixing in the Labrador and Greenland Seas reduces and the AMOC weakens. As the winter sea ice edge retreats farther into the regions with high surface freshwater content in the central Arctic Basin, the mixing becomes shallower and the ArMOC weakens. Our results suggest that the location of deep-water formation plays a decisive role in the structure and strength of the ArMOC; however, the intermittent strengthening of the ArMOC and convection north of the Greenland–Scotland ridge cannot compensate for the progressive weakening of the AMOC.

KEYWORDS: Ocean; Arctic; Deep convection; Meridional overturning circulation; Ice loss/growth

1. Introduction

Arctic sea ice cover has retreated at an unprecedented rate in the last decades as a consequence of rising greenhouse gases (Nghiem et al. 2007; Notz and Stroeve 2016; Stroeve and Notz 2018). As a consequence of the warming, the deep convection in the Labrador Sea is weakening (Yang et al. 2016). Under further emissions, these trends are expected to continue, ultimately resulting in a seasonally ice-free Arctic (Notz and Community 2020) with a potential shut down of North Atlantic deep-water formation (Jahn and Holland 2013; Brodeau and Koenigk 2016). On a larger scale and related to the reduction in North Atlantic deep-water formation, a weakening of the Atlantic meridional overturning circulation (AMOC) is found in most climate models (Cheng et al. 2013). However, little is known about potential changes in the deep circulation and overturning in the Nordic seas and Arctic Ocean.

Winter in the high latitudes is characterized by strong heat fluxes from the relatively warm ocean to the much colder atmosphere, destabilizing the upper ocean. Depending on the intensity of these fluxes, and the background ocean stratification, the surface cooling is either followed by sea ice formation, inhibiting further ocean heat loss, or compensated by mixing with deeper and relatively warmer ocean water. In the North Atlantic, the high salinity of the upper ocean results in a weak stratification that allows for deep mixing during winter as the surface cools. In contrast, in the Arctic Basin (including the Canadian and Eurasian Basins) there is a fresh surface layer fed by continental river runoff and maintained by the presence of sea ice that currently inhibits open-ocean convection. However, the ongoing warming of the Arctic and the resulting acceleration of the hydrological cycle (Rawlins et al. 2010) and winter sea ice decrease are expected to impact the Arctic stratification (Nummelin et al. 2015; Davis et al. 2016). This might impact the potential for open-ocean convection in the Arctic Basin in the future.

Observations over the past 20 years show that mixing at the end of the winter can reach a depth of 1000 m in areas of the Labrador Sea (Våge et al. 2009; Yashayaev and Loder 2017), the Irminger Sea (de Jong and de Steur 2016), and the Greenland Sea (Brakstad et al. 2019). These deep-water formation sites are the main sources of dense water contributing to the renewal of North Atlantic Deep Water and, thus, setting the strength of the AMOC. However, the convection strength varies in time. While deep convection can disappear for a few years, as in the Labrador Sea during the Great Salinity Anomaly in the 1960s (e.g., Kim et al. 2020), it can also be absent for longer time periods, as for the last interglacial

Denotes content that is immediately available upon publication as open access.

Corresponding author: Anaïs Bretones, anais.bretones@uib.no

DOI: 10.1175/JCLI-D-21-0152.1

(Hillaire-Marcel et al. 2001). Under future global warming, deep convection in the North Atlantic and the AMOC is predicted to weaken (Cheng et al. 2013; Jahn and Holland 2013). This raises concerns, as the intensity of the convection and the production of dense water influences how much heat and carbon are stored in the deep ocean. In particular, changes in deep-water formation have previously been associated with major climate shifts, such as the Heinrich events (Broecker et al. 1992) and the Young Dryas (Fairbanks 1990).

In contrast to studies focusing on the shutdown of Labrador Sea deep-water formation under increased freshwater fluxes into the subpolar gyre, Lique et al. (2018) link deep-water formation changes, in particular enhanced convection in the Arctic, to winter sea ice retreat. Under $4 \times CO_2$ forcing in the High-Resolution Global Environmental Model (HiGEM), the authors find a northward shift of the deep mixing regions (defined by a mixed layer deeper than 400 m), corresponding to the northward retreat of sea ice. The simulated sea ice retreat is found to be associated with a change in surface circulation, bringing more salty Atlantic water into the Eurasian Basin and weakening the upper ocean stratification. Under this configuration, enhanced air–sea buoyancy fluxes, facilitated by the retreat of the sea ice, deepen the mixed layer.

The findings of Lique et al. (2018) shed new light on an earlier study by Bitz et al. (2006) with the Community Climate System Model, version 3 (CCSM3). Using a transect crossing the Arctic region to compute the overturning circulation, Bitz et al. (2006) find a strengthening of the overturning north of the Greenland–Scotland ridge in an experiment with a doubling of CO_2. The enhanced circulation is linked to increased sea ice production in the Arctic Ocean, from the Siberian Shelf to the Canadian Archipelago. Studying the simulated ocean ideal age, Bitz et al. (2006) identify anomalously young water on the Siberian shelf, indicating strengthened convection, possibly impacting the Arctic overturning. The authors do not assess changes to the depth of the mixed layer in the new ice-free open ocean regions. However, it is plausible that enhanced deep convection in these regions could be an alternative explanation for the simulated strengthened Arctic overturning.

Rather than applying an instant doubling or quadrupling of atmospheric CO_2 as in Lique et al. (2018) and Bitz et al. (2006), Brodeau and Koenigk (2016) apply an emission scenario with gradually increasing CO_2 (RCP8.5), to observe how the deep convection in the Arctic follows the retreating winter sea ice. They forecast a shutdown of the deep convection in the Labrador Sea and Iceland–Scotland area by the early 2020s using an ensemble of 12 simulations with EC-Earth3. Starting at this time, convection in the Nordic seas weakens, and by 2060 it is replaced by convection in the Arctic Ocean. This evolution is consistent with the northward shift of deep-water formation suggested by Lique and Thomas (2018). However, in all the aforementioned studies, the model simulations end before the winter sea ice is completely gone; making it impossible to investigate if deep convection develops further into the Canadian and Eurasian Basins, and how it relates to the Arctic overturning. Moreover, these previous studies do not account for the impact of increasing freshwater fluxes from the Greenland ice sheet that can inhibit convection (Fichefet et al. 2003). Depending on where the freshwater is transported and stored, increased freshwater fluxes could have major impacts on deep-water formation and overturning circulation by strengthening upper ocean stratification and inhibiting deep convection (Smith and Gregory 2009; Böning et al. 2016).

Here, we study the northward shift of deep convection and its link to winter sea ice retreat under the RCP8.5 scenario using a long simulation with EC-Earth coupled with a dynamic Greenland ice sheet. By introducing a new metric for the overturning circulation in the central Arctic Ocean, we discuss the impact of enhanced Arctic overturning on the large-scale AMOC. Moreover, the exceptional length of the coupled EC-Earth experiment results in a year round ice-free Arctic, making it possible to study the long term fate of Arctic deep-water formation and overturning.

2. Methods

In this study, we analyze a projection from the EC-Earth–Parallel Ice Sheet Model (PISM), a state-of-the-art climate model with a dynamical ice sheet module for the Greenland ice sheet (Madsen et al. 2020, manuscript submitted to *Climate Dyn.*). EC-Earth-PISM is built on the climate model EC-Earth, version 2.3 (Hazeleger et al. 2012, herein referred to as EC-Earth2.3), which is coupled with (PISM (Bueler and Brown 2009; Winkelmann et al. 2011) for the Greenland ice sheet. EC-Earth2.3 is a model developed by the EC-Earth consortium with contributions to phase 5 of the Coupled Model Intercomparison Project (CMIP5). It consists of the ECMWF's Integrated Forecast System (IFS) model cycle 31r1 (https://www.ecmwf.int/en/publications/ifs-documentation) with updated physical parameterizations, the Nucleus for European Modeling of the Ocean version 2.2 (NEMO2; Madec 2008) developed by L'Institut Pierre-Simon Laplace (IPSL) embedded with the Louvain-la-Neuve Sea Ice Model, version 2 (LIM2; Fichefet and Maqueda 1997), and the Ocean Atmosphere Sea Ice Soil coupler, version 3 (OASIS3; Valcke 2006).

In EC-Earth-PISM, the atmosphere is modified to represent surface processes over the ice sheet. The coupling with the PISM ice sheet model involves an exchange of information between the atmospheric component of EC-Earth2.3 and PISM without anomaly or flux corrections. The simulated monthly surface temperature and mass balance over the Greenland ice sheet are passed on to PISM and drive the dynamics and thermodynamics of the ice sheet. In exchange, the simulated ice mass changes in PISM are returned to EC-Earth2.3 as changes to ice extent and ice topography influencing the atmospheric circulation (Madsen et al. 2020, manuscript submitted to *Climate Dyn.*), and as freshwater fluxes influencing the ocean circulation. Thus, the model simulates the climate induced changes to the Greenland ice sheet, as well as their resulting coupled feedbacks. In particular, Madsen et al. (2020, manuscript submitted to *Climate Dyn.*) found that under a $4 \times CO_2$ increase, freshwater fluxes from the Greenland ice sheet increase by 65% when EC-Earth is coupled with PISM. In fact, surface melting is enhanced by the snow–albedo feedback in EC-Earth-PISM. In addition, the EC-Earth-PISM has a fresher top layer in the Arctic, a more extensive winter sea ice

TABLE 1. Characteristics of the scenario simulations used in this study. Note that the uncoupled simulation stops at 2100, limiting the possibilities for comparison between the two simulations. Every figure is based on the EC-Earth-PISM simulation (boldface text), except Figs. 1 and 9, which also show the EC-Earth simulation (gray lines).

Model name	Model versions	Emission scenario	Scenario simulation	Reference
EC-Earth	EC-Earth2.3	RCP8.5	2006–2100	Hazeleger et al. (2012), Koenigk et al. (2013)
EC-Earth-PISM	**EC-Earth2.3 coupled with PISM (dynamic Greenland ice sheet)**	**Representative&Extended Concentration Pathway 8.5 (RCP&ECP8.5)**	**2006–2300**	Madsen et al. (2020, manuscript submitted to *Climate Dyn.*)

cover, weaker overturning at 26°N and cooler surface air temperature after the equilibrium is reached.

Following the EC-Earth2.3 configuration for CMIP5, EC-Earth-PISM has a horizontal spectral resolution of T159 in the atmosphere with physical processes on a linear reduced Gaussian of about 125 km × 125 km, and 62 vertical layers. For the ocean, the horizontal resolution is about 1° with 42 vertical levels, and a horizontal refinement to one-third of a degree near the equator resolving equatorial planetary waves. PISM uses a regular polar-stereographic grid at 20-km resolution.

The EC-Earth-PISM experiment analyzed in this study is a long climate change simulation following the CMIP5 protocol (Taylor et al. 2012) for the historical period (1850–2005), and the representative concentration pathway 8.5 scenario for the future projection period (2006–2300). This scenario is based on an increase in emissions leading to a radiative forcing of 8.5 W m^{-2} by 2100. Following 2100, the emissions are stable for 50 years before they are considerably reduced from 2150 to 2250, resulting in a stabilization of the radiative forcing at 12.5 W m^{-2} from 2250 to 2300 (van Vuuren et al. 2011).

The experiment started from a multicentury control run with preindustrial boundary conditions, for which the global mean surface temperature and the Greenland ice sheet remain in a quasi-stable state (Madsen et al. 2020, manuscript submitted to *Climate Dyn.*). The experiment continues after 2300 for another 900 years until the year 3200, while keeping the radiative forcing constant at the 2250 level (12.5 W m^{-2}). In this study we focus on the period 1950–2300, investigating changes in ocean circulation and deep convection during Arctic sea ice retreat and Greenland ice melt. For comparison, we include the CMIP5 historical and RCP8.5 experiment (from 1850 to 2100) with EC-Earth2.3 (referred to as EC-Earth) without the coupling to the PISM ice sheet model. Table 1 summarizes the differences between the two simulations used in this study.

3. Results

a. Sea ice decrease

As the EC-Earth-PISM experiment continues after the year 2100, it captures the disappearance of Arctic sea ice in both summer and winter. Figure 1 shows the evolution of the sea ice extent, defined as the area with a concentration of sea ice higher than 15%, in September (summer) and March (winter) from 1950 to 2300. The summer sea ice reduction accelerates around year 2040, resulting in an ice-free ocean (sea ice extent < 1 M km^2, where M $= 10^6$) in the summer from year 2060. A similar abrupt reduction of the winter sea ice occurs in year 2135, leaving the Arctic Ocean perennially ice free from year 2165.

The abrupt summer reduction in sea ice is similar for the experiment without the dynamic Greenland ice sheet (gray lines in Fig. 1). Until 2100, the winter sea ice extent decreases at the same rate in EC-Earth-PISM and EC-Earth. This suggests that the coupling with a dynamic ice sheet does not modify the timing of the sea ice reduction, at least until 2100. However, note that the ice volume change of Greenland, resulting in enhanced freshwater fluxes to the ocean in the coupled experiment, is relatively low before 2100 (gray line, Fig. 2). Unfortunately, the shorter length of the uncoupled (EC-Earth) experiment does not allow us to study how the increasing freshwater fluxes from Greenland influence the winter sea ice reduction after 2100. However, in the complementary 4 × CO_2 forcing experiment with EC-Earth-PISM, Madsen et al. (2020, manuscript submitted to *Climate Dyn.*) found a more extensive winter sea ice cover at equilibrium.

As this study primarily focuses on processes occurring during sea ice retreat, we mainly focus on three time periods

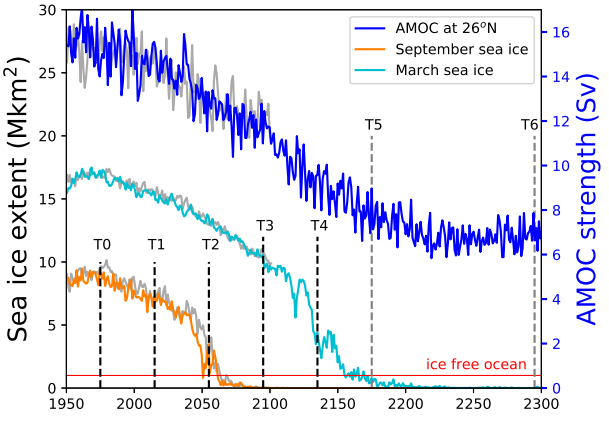

FIG. 1. Time series of the AMOC index (maximum transport at 26°N) and Arctic sea ice extent in March (light blue) and September (orange) from 1950 to 2300 for EC-Earth-PISM. Superimposed in gray from 1950 to 2100 are the same variables for the run that does not include the dynamic Greenland ice sheet. The red line indicates ice-free ocean conditions (sea ice extent < 1 M km^2, M $= 10^6$). The main time periods used in this analysis are indicated with dotted lines centered on each time period. T0 is used in Fig. 7 and T1 is used in Fig. 4, while T0, T2, T3, and T4 are used in Figs. 3, 6, 8, 10, and 12, and T3, T4, and T5 are used in Fig. 11.

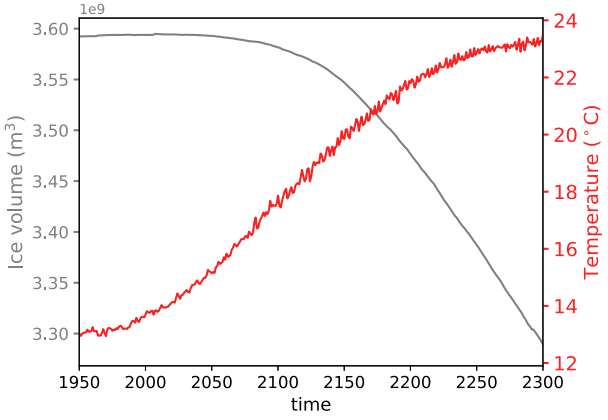

FIG. 2. Global mean annual surface air temperature (red) and Greenland ice volume (gray) in the EC-Earth-PISM simulation under the RCP8.5 emission scenario. The Greenland ice volume change results in freshwater fluxes to the ocean (see Fig. A1).

evenly spaced from 2050 to 2140: 2050–60 (T2), 2090–2100 (T3), and 2130–40 (T4), with results from each period averaged over 10 years. These are compared with the time period 1970–80, which is referred to as the historical period (T0). In addition, the period 2010–19 (T1) is used in section 3b to compare the model run with observed mixed layer properties, and the periods 2170–80 (T5) and 2290–2300 (T6) are used in section 3f to investigate the long-term evolution of an ice-free Arctic Ocean. Note, however, that the time periods T4, T5, and T6 are outside the range of the uncoupled EC-Earth simulation.

Each time period is distinct, with the mean position of the summer and winter sea ice edge progressing further into the central Arctic Ocean as the climate warms (Fig. 3). From T0 to T2, the summer sea ice edge retreats from the Barents, Kara, and Laptev Seas, as well as the Chukchi and East Siberian Seas (orange line, Fig. 3b). As shown in the time series of sea ice extent, the remaining summer sea ice is gone by the end of T2, leaving the Arctic Ocean ice free during summer for both T3 and T4 (Figs. 3c,d). On the other hand, winter sea ice (blue line) prevails in all four time periods. From T0 to T2, the winter sea ice edge retreats from most of the Barents Sea (Fig. 3b). A small reduction is found in the Greenland and Iceland Seas, but the sea ice edge still reaches Svalbard, Iceland, and the southern coast of Greenland. During T3, the retreat is visible in the Labrador Sea, along the east coast of Greenland, around Svalbard, and farther north in the Kara Sea and into the Eurasian Basin (Fig. 3c). During T4 the retreat accelerates with the opening of a large passage connecting the Greenland, Barents, and Kara Seas with the Chukchi Sea (Fig. 3d). Although the winter sea ice area does not change much from the historical period T0 to T2 or T3, it should be noted that the sea ice thins considerably. While the sea ice is up to 8 m thick during T0, it does not exceed 1.5 m during T3 (Fig. 3), which is explained by the lack of multiyear ice as the sea ice disappears completely during summer (Fig. 1). Finally, the winter sea ice retreat is accompanied by a warming of the surface ocean.

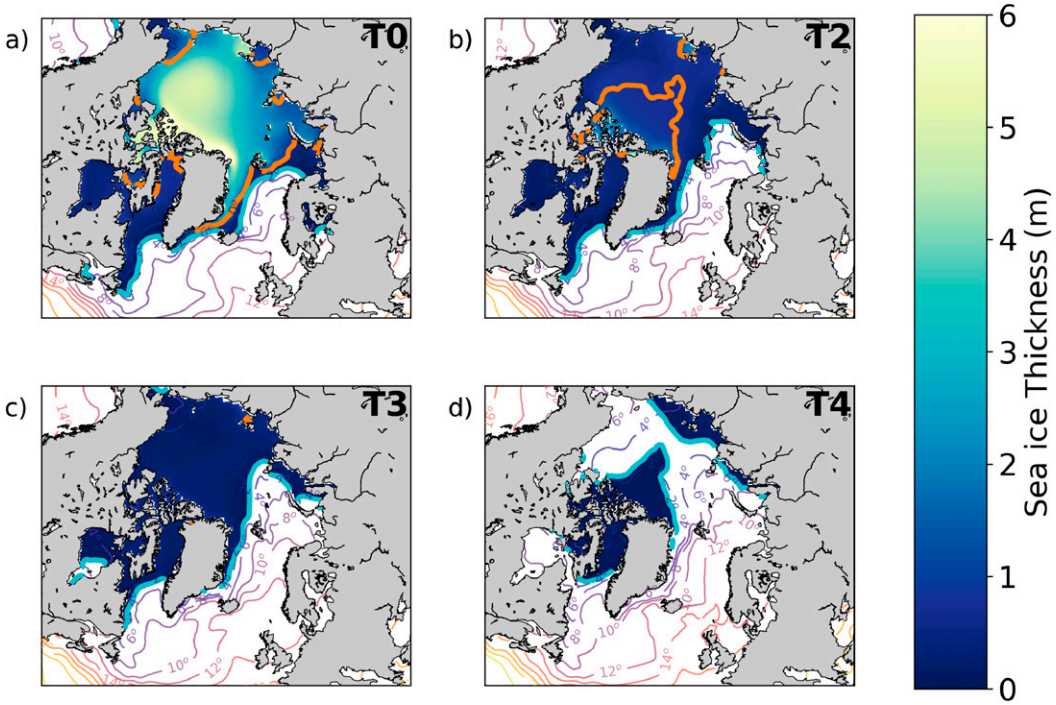

FIG. 3. Yearly mean sea ice thickness (shading; see color bar) and sea surface temperature (contour lines) for (a) T0: 1970–80, (b) T2: 2050–60, (c) T3: 2090–2100, and (d) T4: 2130–40 in the EC-Earth-PISM simulation. The blue line indicates the sea ice edge in March (winter) and the orange line marks the sea ice edge in September (summer). The sea ice edge corresponds to the 15% sea ice concentration contour line.

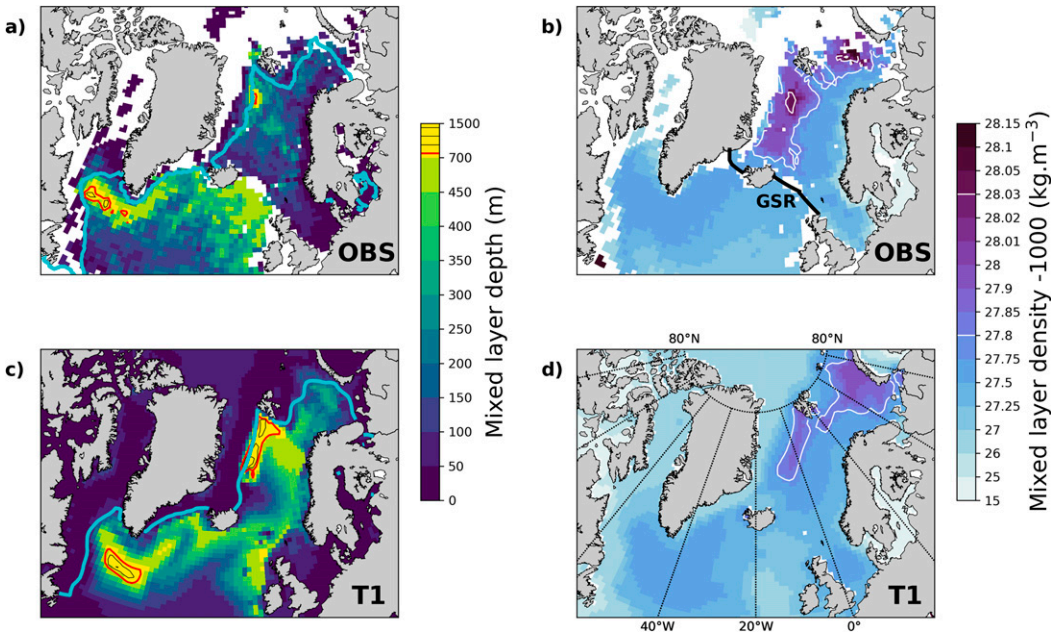

FIG. 4. Mixed layer depth with (a),(c) sea ice extent (blue line) and (b),(d) mixed layer density averaged over three winter months (February–April) for the time period T1: 2010–19. The red contour lines highlight the regions with an 800-m-deep mixed layer. The white contour lines indicate densities of 1027.8 and 1028.03 kg m^3. The sea ice extent in (a) was obtained from the National Snow and Ice Data Center (NSIDC). Mixed layer properties in (a) and (b) are based on observations, while (c) and (d) are EC-Earth-PISM model outputs.

In particular, the Barents Sea experiences a warming of 6°C from T0 to T3. At the same time, the warming in the Labrador Sea, where the sea ice edge retreat is smaller, is limited to 2°C.

b. Deep convection regions at present (T1)

The changing sea ice cover during the model simulation affects both the strength and position of wintertime convection. Before we investigate these changes further, we evaluate to what extent EC-Earth-PISM captures deep convection at present by comparing simulated mixed layer depth and density to observations for the period 2010–19 (Fig. 4). Both the observed and simulated mixed layer depth is identified as the depth where the density reaches $\rho(T_0 - \Delta T, S_0)$ where T_0 and S_0 are the surface temperature and salinity, respectively, and $\Delta T = 0.2$°C following de Boyer Montégut et al. (2004) and Holte et al. (2017). The corresponding mixed layer density is estimated as the average potential density over the extent of the mixed layer. Modeled mixed layer depths were computed using monthly averages of temperature and salinity. Observed mixed layer properties based on Argo float profiles were collected from Holte et al. (2017) south of the Greenland–Scotland ridge (indicated by the black line in Fig. 4b). Mixed layer estimates north of the ridge were obtained using observations from the dataset combined by Huang et al. (2020). This dataset includes shipboard hydrographic profiles and was used to achieve a good spatial coverage in the Barents and Nordic seas (in regions with limited Argo float data). All mixed layer properties are estimated for individual profiles before they are averaged over February, March, and April, which is when the deepest convection typically occurs. Averaging over a 3-month period also increases the number of observations, hence the reliability of the observational mixed layer climatology. Finally, we interpolate the observations onto our model grid for comparison with the modeled mixed layer depth.

The Labrador Sea and Greenland Sea stand out with observed mixed layers deeper than 1000 and 800 m, respectively (Fig. 4a). In EC-Earth-PISM, the deepest mixed layers are found in the same two regions (Fig. 4c); however, these convective regions are broader, especially in the Greenland Sea where the area of deep mixing extends south to the Iceland Sea. On average, EC-Earth-PISM tends to have deeper mixed layers, with a larger area depicting a mixed layer exceeding 500-m depth (e.g., east of the Greenland Sea or south of the Greenland–Scotland ridge). For the purpose of this study, we divide the North Atlantic and Arctic deep-water formation sites into four regions (Fig. 5): the Labrador Sea (between 60° and 35°W), the Iceland–Scotland region (south of Iceland and along the Greenland–Scotland ridge, as in Brodeau and Koenigk 2016), the western Nordic seas (Greenland and Iceland Seas) and the Nansen Basin (north of the Barents Sea). The deep-water formation sites are defined as areas with a mixed layer deeper than 800 m (red contour line in Figs. 4c and 6).

The deep convection sites in the western Nordic and Labrador Seas are associated with high mixed layer densities. Both the pattern and magnitude of the mixed layer density are well represented by the EC-Earth-PISM simulation (Figs. 4b,d), especially in the western Nordic seas (see the white contour indicating a mixed layer density of 1027.8 kg m^{-3}). One exception is the lack of the very dense mixed layers in the central

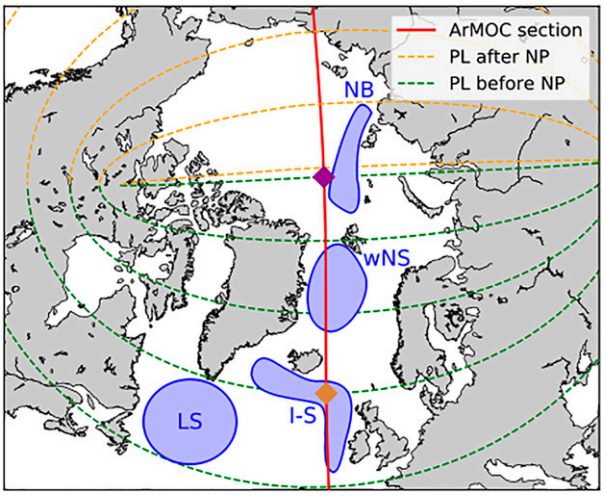

FIG. 5. Location of the dense-water formation regions used in this paper: Labrador Sea (LS), Iceland–Scotland (I-S), western Nordic seas (wNS), and Nansen Basin (NB). The red line indicates the section used in Figs. 8 and 10 and the purple and brown diamonds the position of the triangles in these same figures. The green and orange lines show the pseudolatitudes (PL) used to compute the ArMOC: for one PL, velocities perpendicular to that PL (pseudomeridian velocities) are integrated from America to Europe.

Greenland Sea, where observations indicate a density exceeding 1028.03 kg m^{-3}. On the other hand, the mixed layer density in the Labrador Sea is slightly higher in EC-Earth-PISM than in the observation based climatology. Despite small differences (slightly deeper and broader convective regions), the model represents the overall pattern of deep convection and the formation of dense water masses well. In the following we will study how these features evolve with time.

c. *Weakening and migration of deep convection regions*

The mixed layer changes dramatically from T0 to T4 as the winter sea ice retreats (T1 not shown in this section). This is seen by superimposing the March mixed layer depth with the March sea ice extent for T0, T2, T3, and T4 (Fig. 6). During T0 (Fig. 6a), deep convection is present in the Labrador Sea (>1500 m), in the western Nordic seas (1100 m) and in the Iceland–Scotland region (800 m), similarly to T1 (Fig. 4c). The magnitude of convection cannot be directly compared with Fig. 4c since it is averaged over March only (instead of February, March, April). Still, a similar pattern can be recognized. In general, there is a clear contrast in mixed layer depth between the regions close to the sea ice edge and those covered by sea ice where only shallow (<100 m) mixing occurs. The main difference between T0 and T1 is a northward shift in regions showing the deepest convection. During T0 the mixed layer depths in the southernmost regions (Labrador Sea and Iceland–Scotland) exceed those in the western Nordic seas, which is opposite to what was found for T1 (Fig. 4c).

For T2 (Fig. 6b), there is no active deep-water formation in the Labrador Sea and the Iceland–Scotland region since, in these regions, the maximum mixed layer depth is reduced to 450 m. The remaining active deep-water formation areas are farther north in the western Nordic seas. A decline in the maximum mixed layer depth is also found in the Nordic seas, although to a lesser extent than in the Labrador Sea. Within the western Nordic seas, the location of the deepest mixed layer depth moves north to the south coast of Svalbard, following the retreating winter sea ice edge. This supports the hypothesis that deep-water formation sites are migrating northward, as the climate warms and the winter sea ice edge retreats. Given the reduction in deep-water formation area and mixed layer depth, the amount of deep water formed is also reduced.

The northward migration continues in T3 (Fig. 6c) with 900-m deep convection appearing north of Svalbard at the edge of the winter sea ice cover in the Nansen Basin. Farther south, mixed layers in the three original convective regions are shallower with only one active convection site left in the western Nordic seas. The northward progression stops during T4 (Fig. 6d). Neither the Nordic seas nor the Nansen Basin have convection exceeding 700 m, and the sea ice edge decouples from the deepest mixed layer regions. As a result, the T4 period and the rapid retreat of winter sea ice marks the end of the North Atlantic deep-water formation era.

d. *AMOC weakening at 26°N*

Deep convection is thought to be important for the strength, structure, and variability of the AMOC (Kuhlbrodt et al. 2007). Here, we review the main characteristics of the AMOC in EC-Earth-PISM for easy comparison with other studies.

The AMOC can be seen as the superposition of two cells turning in opposite direction in the depth-latitude space, and visualized via the streamfunction Ψ:

$$\Psi(\lambda, z) = \int_0^z \int_{\text{west}}^{\text{east}} V(\phi', \lambda, z')\, d\phi'\, dz', \tag{1}$$

where V is the meridional velocity, ϕ is the longitude, λ is the latitude, and z is the depth. In the following, we focus on the upper cell that transports warm Atlantic water northward and cooled ventilated water at depth southward.

For T0 in EC-Earth-PISM, the upper cell of the overturning is located between 200- and 2500-m depth (Fig. 7) with a core at 900-m depth and a maximum transport of 15 Sv (1 Sv $\equiv 10^6$ m^3 s^{-1}). The northward flowing Atlantic water returns to depth south of the Greenland–Scotland ridge (60°–68°N), apart from 2 Sv, which sinks north of the ridge before returning southward to merge with the main AMOC cell at 800–1000-m depth (white contour in Fig. 7). The accuracy of the overturning meridional streamfunction north of the Greenland–Scotland ridge will be addressed in section 3e.

For ease of comparison, it is common to compute Ψ at 26°N, which is also the latitude of the 19 moorings deployed in 2004 as part of the RAPID program (Cunningham 2008). The maximum strength of the meridional overturning streamfunction at 26°N is often used as an AMOC index. Based on the RAPID array, McCarthy et al. (2015) evaluated the AMOC index to be 17.2 ± 4.6 Sv between 2004 and 2007. For this same time period, EC-Earth-PISM has a mean AMOC index of 14.4 Sv (Fig. 1), which is within the observed uncertainty range.

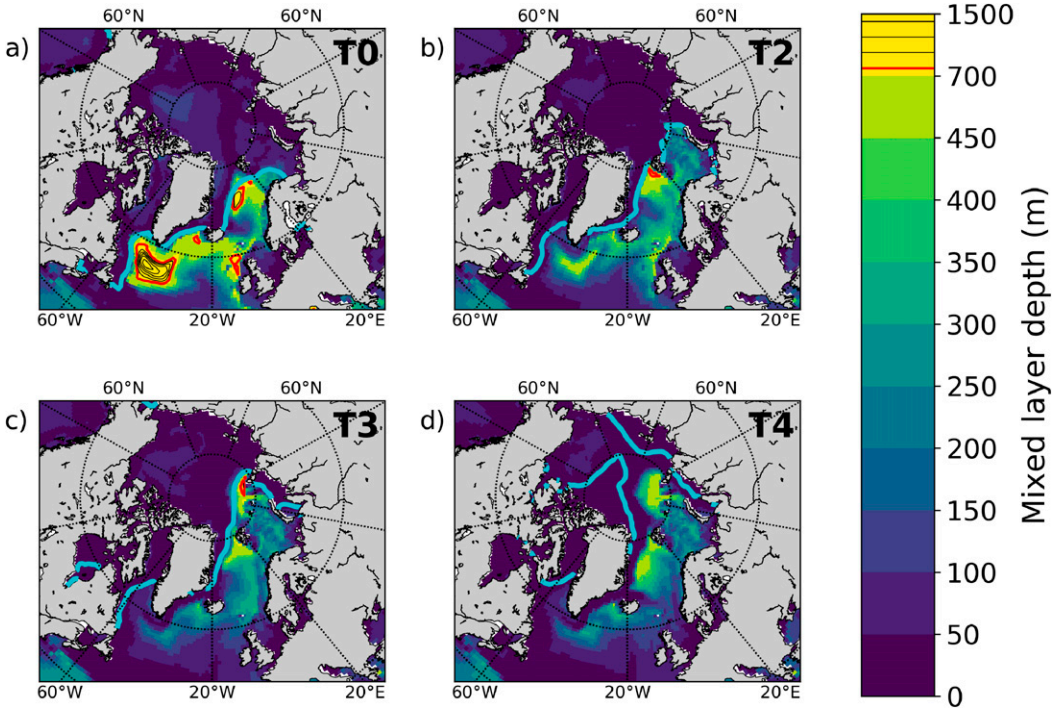

FIG. 6. Mixed layer depth in March for the four different time periods in the EC-Earth-PISM simulation. The blue line indicates the winter sea ice extent and black contour lines indicate mixed layer depths greater than 800 m.

However, following the simulated decline in deep convection, the modeled AMOC is expected to weaken. Similar to 10 other CMIP5 models showing a 15%–60% AMOC index weakening at 30°N by 2100 (Cheng et al. 2013), we record a weakening of 22% by 2100 and 55% by 2200 at 26°N. Following 2200, the AMOC index increases slightly before stabilizing at a mean value of 7 Sv for the remainder of the experiment (until the year 3200, not shown here). The coupled and the uncoupled experiments show the same AMOC changes (blue vs gray in Fig. 1) until 2100. However, Madsen et al. (2020, manuscript submitted to *Climate Dyn.*) show that the recovery following the weakening of the AMOC is reduced in EC-Earth-PISM with respect to EC-Earth.

e. Strengthening of the ArMOC

The meridional overturning streamfunction [Eq. (1)] is a convenient tool to capture the mean water-mass transport in the Atlantic; however, it is not well adapted to the Arctic Basin where integration over longitude is no longer constrained by continents. The result of the integration at 75°N includes for example the transport in the Greenland Sea and the transport in the East Siberian Sea, which are separated by the Eurasian Basin and at opposite longitudes. Hence the transport at 75°N is based on very distinct regions that also have opposite positive meridional velocities. Therefore, the meridional overturning streamfunction may not be a physically correct estimate for the overturning at high latitudes, and the secondary AMOC cell north of 65°N (Fig. 7) may be underestimated.

To further investigate changes in the meridional overturning at high latitudes, we calculate the overturning by integrating the velocities along a transect going from Iceland to the Siberian shelf following Bitz et al. (2006) (see red line in Fig. 5). Here, we use a similar domain of integration by making use of the segment pole of the EC-Earth-PISM's ocean model's ORCA grid (see Madec 2008 for details). On the ORCA grid the variables are defined on pseudolatitudes that flatten close to the North Pole becoming parallel to the Alaska–Siberia segment pole. We integrate v, the velocities normal to the pseudolatitude before the North Pole (green lines in Fig. 5), and continue with $-v$, the velocities normal to the pseudolatitude after the North Pole (yellow lines in Fig. 5) and

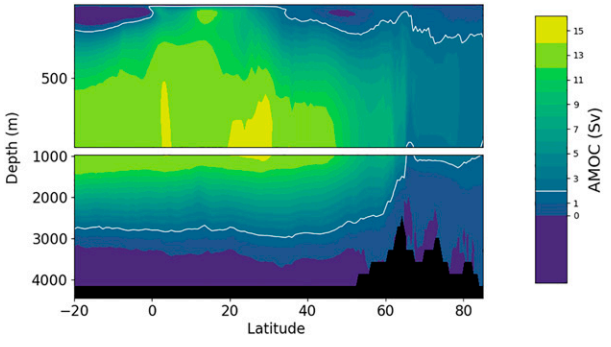

FIG. 7. AMOC during T0: 1970–80 as shown by the meridional overturning streamfunction from 20°S to 90°N in the EC-Earth-PISM simulation. The white contour line (2-Sv transport) stresses a weak northern extension of the AMOC, past the Greenland–Scotland ridge at 65°N.

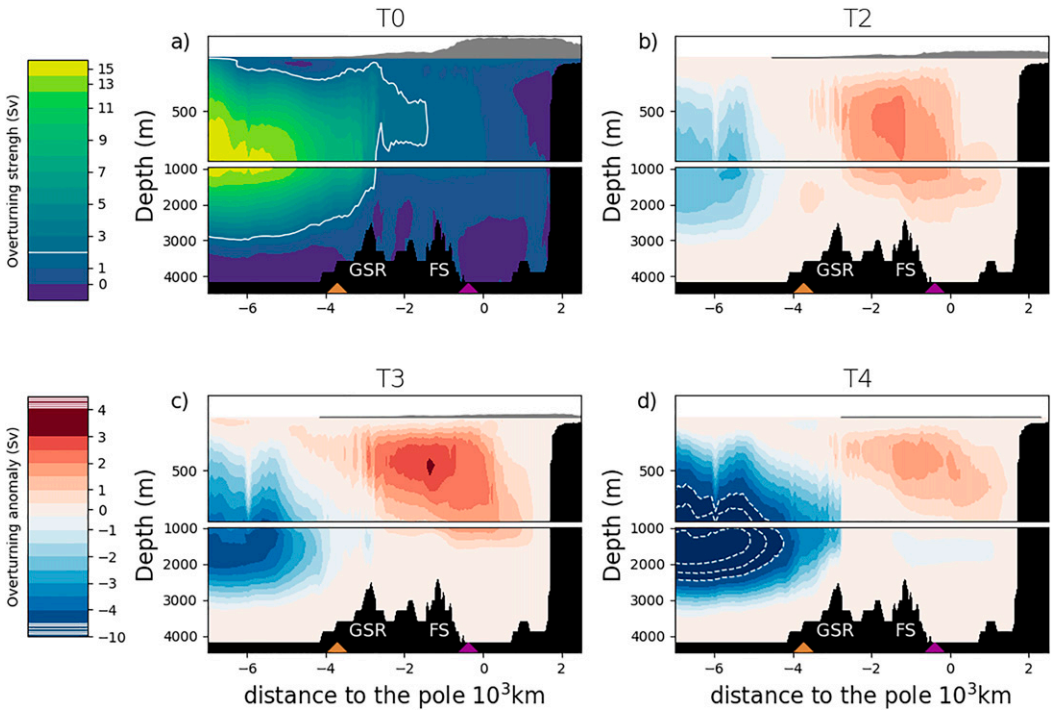

FIG. 8. ArMOC during (a) T0: 1970–80 and anomalies during (b) T2: 2050–60, (c) T3: 2090–2100, and (d) T4: 2130–40 with respect to T0 in the EC-Earth-PISM simulation. Positive anomalies indicate an enhancement of the circulation. In addition to the strengthening of the ArMOC, note the weakening of the AMOC south of the Greenland–Scotland ridge (-7 to -3×10^3 km to the pole). As in Fig. 7, the white contour line at T0 (a) highlights the 2 Sv streamline. For T2, T3, and T4, the white solid (dashed) lines indicate streamlines above 5 Sv (below -5 Sv). The absolute values are shown in Fig. A4. The gray shading at the top of each panel indicates the mean March sea ice thickness as a function of pseudolatitude. The locations of the Greenland–Scotland ridge (GSR) and Fram Strait (FS) are indicated (see also Fig. 5, with matching colors, for the positions of the triangles and a definition of the pseudolatitudes). Note that the bathymetry is a result of a zonal average, which makes the Greenland–Scotland ridge appear deeper than it is.

pointing toward the south. By doing this we ensure that we capture the circulation within the Arctic up to the Siberian shelf in a physically correct manner. The result of this integration can be seen in Fig. 8.

During T0 (Fig. 8a), we observe the typical AMOC cell centered at 900-m depth in the North Atlantic (-6×10^3 km to the pole) and extending to the Greenland–Scotland ridge at 65°N (-3×10^3 km to the pole). This is to be expected, as the integration only differs from the meridional overturning streamfunction north of the Arctic circle at 66°N. North of the Greenland–Scotland ridge, 2 Sv of the AMOC makes its way into the Nordic seas and north to the Fram Strait, and returns at 900-m depth where it merges again with the AMOC. We will from now on refer to the secondary cell north of the Greenland–Scotland ridge as the Arctic meridional overturning circulation (ArMOC).

A clear pattern in the circulation changes can be observed from T2 (Fig. 8b): the AMOC weakens and becomes shallower while the ArMOC strengthens and expands toward the Siberian Shelf. The maximum AMOC is reduced by 2 Sv during T2 and by 4 Sv during T3. In contrast, the maximum strength of the ArMOC increases by about 1.5 Sv during T2, and by 1 to 2.5 Sv during T3. Moreover, positive anomalies of 2.5 Sv are observed at the edge of the Eurasian Basin during T2 and up to the North Pole during T3, which indicates a displacement of the ArMOC toward the interior basin of the Arctic.

While the AMOC at 26°N weakens steadily throughout the twenty-first and twenty-second century, the ArMOC experiences a strengthening until 2100 (T3) followed by a weakening (T4). For comparison with the AMOC index at 26°N through time, the maximal strength with time of the ArMOC in the Nansen Basin (pseudolatitude cutting the red section in Fig. 5 at 87°N, purple diamond) is shown in Fig. 9a. While the AMOC at 26°N weakens, the ArMOC strength almost doubles from 2025 to 2100. After 2100–10 the cell weakens to reach its initial state (1.5 Sv) around year 2225. To link the evolution of the AMOC at 26°N and the ArMOC, Fig. 9a includes a time series of the maximal AMOC strength at 60°N (brown curve), just south of the Greenland–Scotland ridge. Consistent with the AMOC at 26°N, the circulation at 60°N weakens during the twenty-first century but at a much slower rate. However, the weakening at 60°N accelerates around 2100, at the same time as the ArMOC

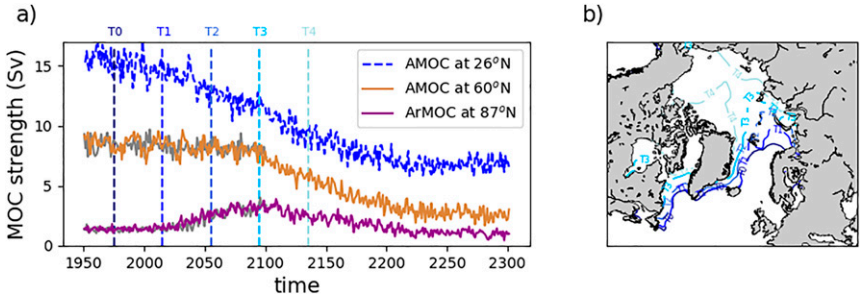

FIG. 9. (a) Time series of the maximal strength of the meridional overturning streamfunction at 26°N in blue (AMOC index), at 60°N in brown, and of the ArMOC at 87°N in purple in the EC-Earth-PISM simulation. Time series for the EC-Earth simulation are superimposed in gray for the AMOC at 60°N and the ArMOC at 87°N. The AMOC at 60°N and ArMOC at 87°N are both computed using the pseudolatitudes outlined in Fig. 5. The main time periods are marked with shades of blue. (b) Map of the ice extent for these time periods with the same colors in (a).

starts to weaken. This suggests that the ArMOC influences the northern overturning circulation in the Atlantic and partly compensates for the early weakening. However, the compensation becomes smaller at lower latitudes and is barely visible in the AMOC strength at 26°N.

This strengthening of the ArMOC until the year 2100 coincides with the northward shift of the ice edge and deep-water formation regions. To investigate this link further, we compute the streamfunction on density surfaces for the ArMOC section. Meridional velocities are collected into potential density bins computed with respect to 2000-m depth and are then integrated throughout the density bins using the cdfmocsig subroutine from the package CDFTOOLS (https://github.com/meom-group/CDFTOOLS).

The result of this integration is shown in Fig. 10a: within the AMOC relatively light water (potential density between 33 and 36.5 $\mathrm{kg\,m^{-3}}$) travels north and return south 3×10^3 km before the pole (~65°N) at density between 36 and 36.8 $\mathrm{kg\,m^{-3}}$. The ArMOC is also associated with a change in density: 2 Sv travel farther north and become even denser reaching a density of 37 $\mathrm{kg\,m^{-3}}$. However, when the dense water formed in the Arctic returns toward the Atlantic and joins the AMOC, the high densities are not conserved. From T2 (Fig. 10b) to T4 (Fig. 10d) the streamfunction anomalies

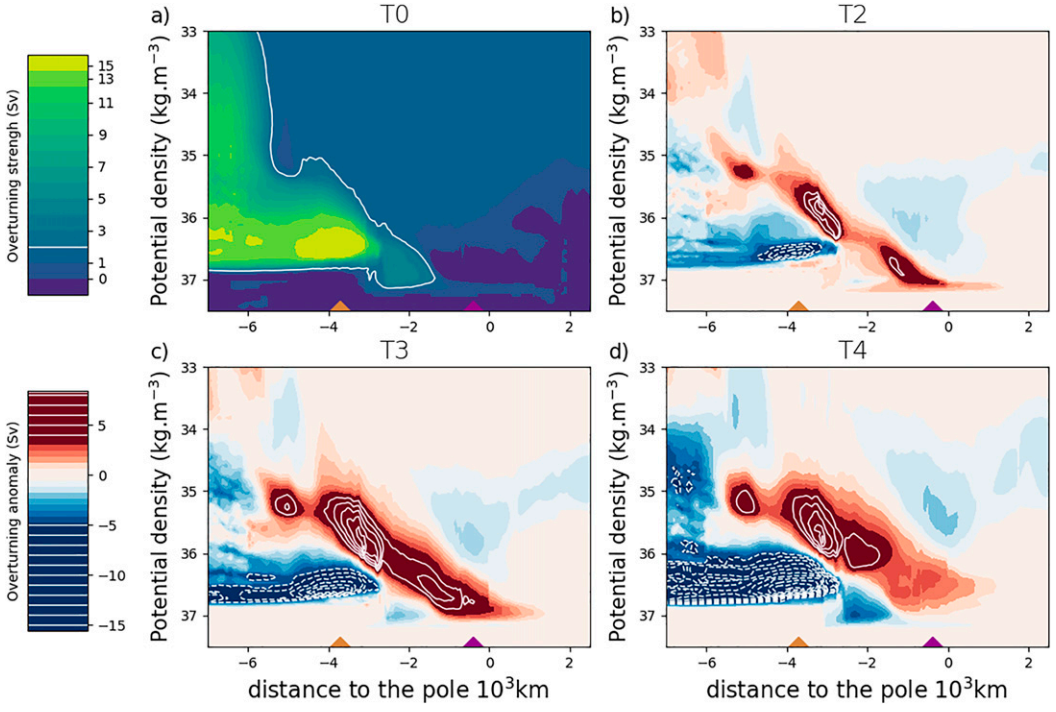

FIG. 10. As in Fig. 8, but in density space. Potential density is computed with respect to the 2000-Pa surface.

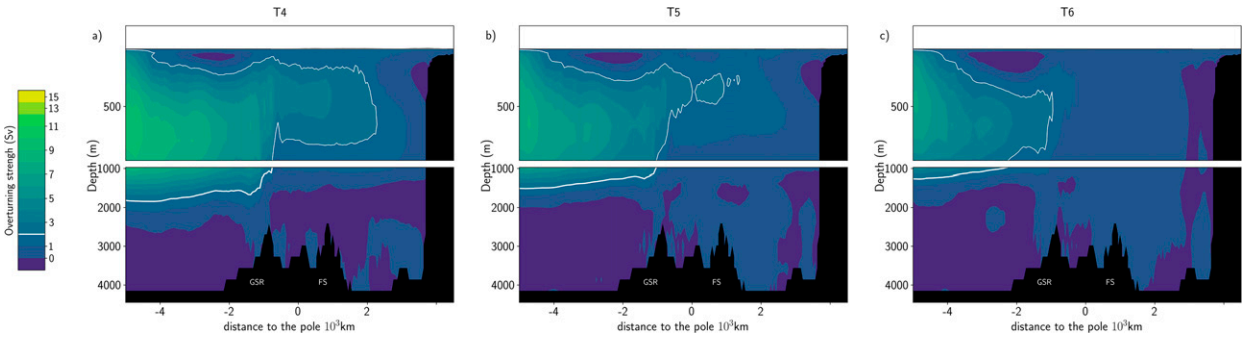

FIG. 11. ArMOC during (a) T4: 2130–40, (b) T5: 2170–80, and (c) T6: 2290–2300 in the EC-Earth-PISM simulation. As in Fig. 7, the white contour lines highlight the 2-Sv streamline.

show two different trends for the AMOC: first the water gets lighter (negative anomaly for the highest densities and positive anomaly for water lighter than 36 kg m^{-3}) and second the overall AMOC weakens. Although more difficult to see than in depth coordinates, it is at least clear during T4 that the circulation has weakened as the weakening in the high density range (10 Sv and more) cannot be compensated by the enhancement observed for the lower densities (5–9 Sv). For the ArMOC, we observe as in Fig. 8 an enhancement of the cell during T2 and T3 together with the development of the cell toward the Siberian Shelf. During T4, Fig. 10d shows that the ArMOC has a weaker core, which is consistent with the streamfunction in depth coordinates.

f. The ice free Arctic Ocean

This section focuses on the changes in the Arctic accompanying the disappearance of the last M km^2 of sea ice. While there is still around 5 M km^2 of winter sea ice during T4, the ocean is ice free by T5 (Fig. 1).

Figure 11 shows that the weakening of the ArMOC initiated between T3 and T4 (Fig. 8) continues after T4: the ArMOC retreats southward between T4 and T5 (Fig. 11b) and the cell is gone by T6 (Fig. 11c). This shows that the simulated weakening of the ArMOC after 2100 (Fig. 9) impacts the entire Arctic overturning cell, from the Greenland–Scotland ridge to the Siberian shelf. The weakening is consistent with the continued reduction in maximum mixed layer depths in the Arctic Basin (not shown).

4. Discussion

Under the most extreme emission scenario from the 5th IPCC report, RCP8.5, Arctic summer sea ice is permanently gone by 2060 in the EC-Earth-PISM simulation (Fig. 1). This timing is independent of the ice sheet coupling: most of the Greenland melting takes place after 2150 (gray line, Fig. A1) when only a small amount of Arctic winter sea ice is left. Additional EC-Earth2.3 experiments by Koenigk et al. (2013) also indicate a summer ice-free ocean from 2060, under the same emission scenario. However, according to Koenigk et al. (2013), the Arctic could be ice free in summer already by 2040 given that the EC-Earth2.3 model overestimates the current observed Arctic sea ice cover, and underestimates the observed retreat rate.

Our coupled simulation also captures the disappearance of winter sea ice, which still covers most of the Canadian and Eurasian Basins by 2100 (T3, Fig. 3). While summer sea ice retreats rapidly from 2035, winter sea ice retreats at a slower rate until the year 2110 (Fig. 1). At this time, the retreat rate increases and the Arctic becomes ice-free all year round from 2165. We focus on the retreat from 1970 to 2130 as the slow winter sea ice retreat appears to be the most relevant for this study.

In addition to the notable sea ice changes in the Arctic, the future of North Atlantic deep convection receives a lot of attention. While many studies focus on the weakening convection in the Labrador and Irminger Seas (Yang et al. 2016; Belonenko et al. 2018), which is forecasted to shut down as a result of increased freshwater fluxes (Jahn and Holland 2013; Wang et al. 2018), it has been suggested that the deep convection could move to higher latitudes, in particular to the interior Arctic Ocean (Nansen Basin; Brodeau and Koenigk 2016; Lique et al. 2018). The latitudinal shift of deep-water formation sites has previously been linked to the winter sea ice retreat by Lique and Thomas (2018) who compared two equilibrium states; one based on preindustrial greenhouse gas concentration with winter sea ice covering the Barents, Greenland, and Iceland Seas, and another based on a 4 × CO_2 increase with respect to preindustrial conditions with the sea ice edge entering the Nansen Basin. More recently, Pérez-Hernández et al. (2019) and Athanase et al. (2020) arrived at the same conclusion after observing deep mixing close to Svalbard in new ice-free areas. Deep convection near Svalbard is a logical intermediate step before it appears in the Nansen Basin; however, the equilibrium simulation by Lique and Thomas (2018) does not allow for an analysis of the changes preceding the emergence of deep convection in the Nansen Basin. Here we opt for an analysis of four time periods of a long coupled experiment covering the different stages of the winter sea ice retreat up to an ice-free Arctic Ocean. Hence, we can test the consistency of deep-water formation changes with winter sea ice retreat in time, and study what happens when the sea ice retreats farther into the Eurasian and Canadian Basins.

We find that as the prevailing deep-water formation sites weaken, new sites appear farther north, closely following the

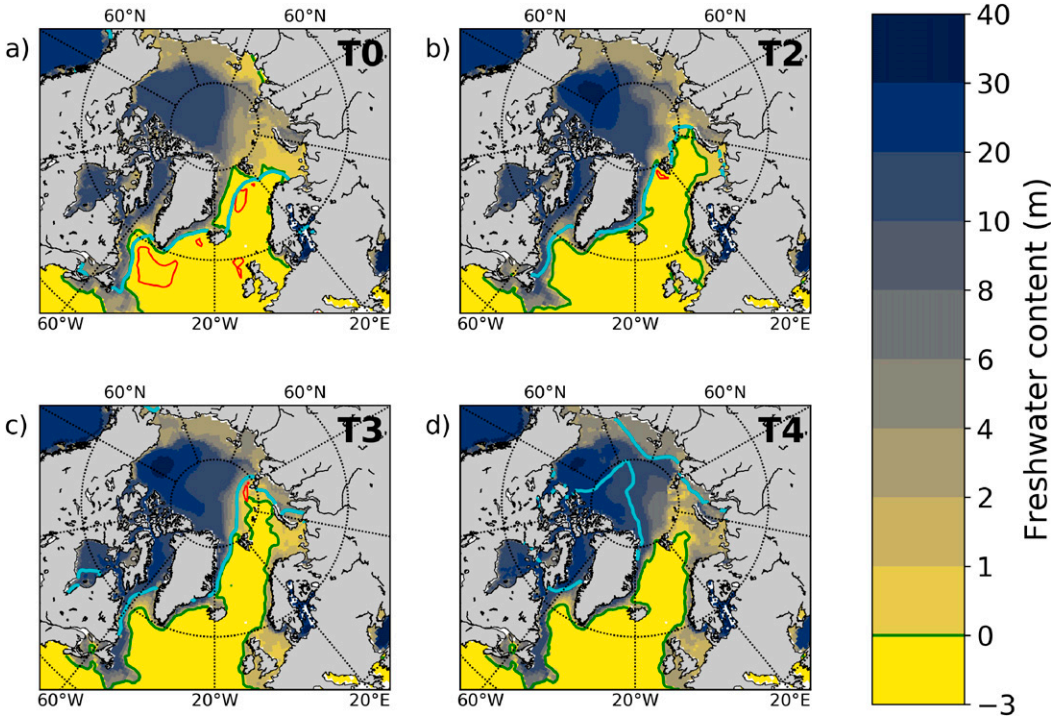

FIG. 12. Freshwater content in the top 800 m during (a) T0: 1970–80, (b) T2: 2050–60, (c) T3: 2090–2100, and (d) T4: 2130–40 in the EC-Earth-PISM simulation. The blue lines indicate the winter (March) sea ice edge, while the red lines indicate the location of deep-water formation.

retreating winter sea ice edge until the sea ice edge reaches the Nansen Basin. At an early stage (T1; 2010–19, Fig. 4c), convection in the Labrador Sea weakens, while convection in the Nordic seas strengthens. In the following years, the core of the convection in the Nordic seas moves farther north to the newly ice free south coast of Svalbard (T2; 2050–60, Fig. 6c), which is consistent with Pérez-Hernández et al. (2019) and Athanase et al. (2020). Finally, the end of the century (T3; 2090–2100, Fig. 6d) is marked by the notable emergence of deep convection in the Nansen Basin at the edge of the winter sea ice cover, as previously described by Brodeau and Koenigk (2016, EC-Earth2.3 with RCP8.5 forcing) and Lique et al. (2018; HiGEM with 4 × CO_2 forcing). Brodeau and Koenigk (2016) show a weakening of the convection in the Nansen Basin toward the end of their simulations (2085 to 2100). What happens after 2100, when the winter sea ice retreats farther into the Eurasian Basin has not been investigated in these previous studies.

According to the long simulations analyzed here, the northward migration of the deep-water formation sites does not continue after 2100. Instead, while the retreat of winter sea ice continues and accelerates, the deepest mixed layers remain within the Nansen Basin and the western Nordic seas during T4 (2130–40, Fig. 6d) and become shallower, consistent with Brodeau and Koenigk (2016). In 2140, 25 years before the Arctic becomes perennially ice free, deep convection (>800 m) is absent in the Atlantic Ocean, in the Nordic seas, as well as farther north in the Nansen Basin. In summary, simulated future reductions in Atlantic deep-water formation is only temporarily and partially compensated by enhanced deep-water formation farther north into the Nordic seas and the Arctic Ocean.

The fact that convection is not initiated in the Canadian Basin can be explained by its high surface freshwater content. The Arctic Ocean, and particularly the Canadian Basin, is known to be very fresh compared to the Atlantic Ocean as a result of river runoff from Siberia and Canada and the inflow of fresh Pacific water through the Bering Strait (Aagaard and Carmack 1989). Here we measure the freshwater content FWC by integrating the salinity anomaly in the upper 800 m, using the reference salinity S_{ref} = 34.8 defined by Aagaard and Carmack (1989) and corresponding to the mean salinity of the Arctic Ocean:

$$\text{FWC} = \int_{-800\,\text{m}}^{0} \frac{S_{\text{ref}} - S(z)}{S_{\text{ref}}} dz .$$

We use a depth of 800 m for the integration and the mean salinity in March to compare the freshwater content with the location of deep-water formation. In EC-Earth-PISM, most of the Arctic Basin has an upper ocean freshwater content larger than 10 m (Fig. 12d). In fact, the presence of freshwater in the top layer indicates that the ocean is highly stratified, hence stable. During T4 (2130–40) the sea ice edge meets this very stable region and the increased air–sea heat flux, in this newly ice-free area, is not sufficient to trigger convection. In contrast, during T3, deep convection in the Nansen Basin was made

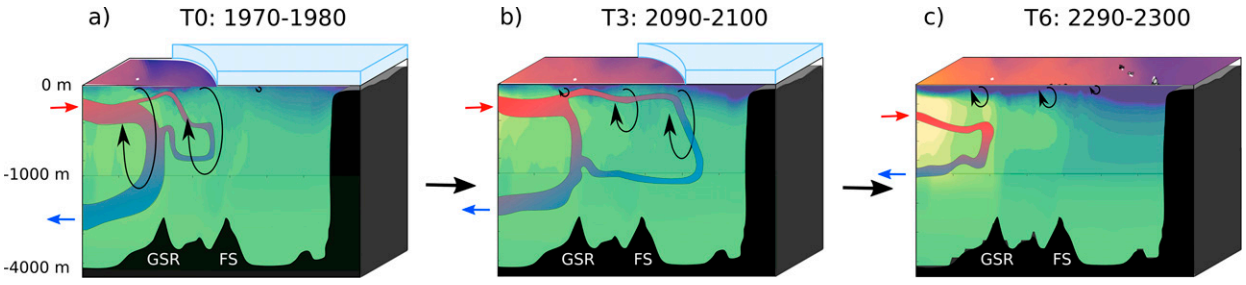

FIG. 13. Sketch summarizing the evolution of the deep mixing and the ArMOC under the retreat of the sea ice edge. (a) During T0: 1970–80 there is deep convection on both sides of the Greenland–Scotland ridge. Both AMOC and ArMOC are present, but the ArMOC extent is limited by the sea ice edge. (b) During T3: 2090–2100 the sea ice edge retreats and the surface ocean warms, which result in shallower (weaker) convection. The ArMOC develops as deep convection moves northward, while the AMOC weakens. Finally, (c) during T6: 2290–2300 there is no more winter sea ice or deep convection, which is linked to the warming of the surface and the freshening of the upper ocean. The AMOC is strongly weakened but still present by opposition to the ArMOC, which has shut down. In this sketch, the ArMOC circulation and the bathymetry are based on Figs. A4a and A4c for T0 and T3 and on Fig. 11 for T6.

possible by a concomitant retreat of freshwater, or intrusion of saline Atlantic water (Fig. 12c). The strengthening of the ArMOC could be responsible for this saline intrusion, which acts as a positive feedback on the ArMOC by weakening the stratification (see the negative Brunt–Väisälä frequency anomaly in the Barents Sea and Nansen Basin; Fig. A2c) and enhancing the convection. However, the saline Atlantic water does not make its way to the central Arctic Basin (Figs. 12d and A3). Most of the Arctic Basin becomes fresher and more stable through time (positive anomaly in Figs. A2b–d). Lique et al. (2018) also obtain stability differences between the Canadian and the Eurasian Basins under the sea ice retreat. They suggest that surface circulation changes in the Arctic Ocean are responsible for the changes in freshwater distribution. Aagaard and Carmack (1989) already suggested that the Eurasian and Canadian Basins could answer differently to the climate change due to their differences in freshwater sources and sinks.

In this study, we find that the changes in deep-water formation in the Nordic seas and Arctic Basin have consequences for the northern extension of the AMOC and introduce the term ArMOC. The ArMOC is shallower than the AMOC and is represented by an overturning of 2–3 Sv (Fig. 8a). However, the ArMOC is associated with a further densification of the Atlantic water (Fig. 10a). As the sea ice and deep-water formation sites retreat northward, the ArMOC strengthens and migrates north (T2, T3, Fig. 8). Moreover, the maximum strength of the ArMOC around 2100 (Fig. 9a) coincides with the disappearance of the northernmost convection site in the Nansen Basin. Bitz et al. (2006) show similar enhancement of an Arctic cell in a CO_2 ramping experiment with CCSM3. However, in this previous study the enhancement is linked to increasing sea ice formation on the Siberian shelf as a consequence of increased seasonality. The timing of increased sea ice formation and the enhanced ArMOC do not coincide in our simulation. Instead, we suggest that open-water convection is the main driver of the Arctic cell.

The strengthening of the ArMOC during the twenty-first century contrasts with the forecasted AMOC weakening. The weakening of the AMOC at 26°N is found in most climate models (Cheng et al. 2013) and is consistent with the reduction in North Atlantic deep convection (Jahn and Holland 2013; Brodeau and Koenigk 2016). However, the observed reduction in deep-water formation has not yet been linked to a consistent observed weakening of the AMOC at 26°N (Smeed et al. 2018). In the long EC-Earth-PISM simulation, the AMOC strength at 26°N steadily decreases from 15.5 Sv in 1950 to 7 Sv in 2200 (Fig. 9a). We find that the ArMOC strengthens due to the simulated enhanced deep-water formation north of the Greenland–Scotland ridge, while the AMOC weakens because of the overall deep-water formation reduction. In particular, the enhanced deep-water formation north of the Greenland–Scotland ridge seems to compensate the AMOC weakening at 60°N according to the kink at 2100 present in Fig. 9a coinciding with the ArMOC maximum. However, the intermittent ArMOC strengthening (~1.8 Sv) is small compared to the overall 8.5-Sv reduction of the AMOC at 26°N in the period from 1950 to 2200, hence the delay is unnoticed at 26°N. Similarly, Lique et al. (2018) estimate an increase of the Arctic contribution to the AMOC of only 0.7 Sv when convection reaches the Eurasian Basin.

We suggest that the enhanced convection in the Arctic Ocean and the strengthening of the ArMOC slows down the weakening of the AMOC. This hypothesis is supported by recent observations highlighting a more active role of the region north of the Greenland–Scotland ridge in determining AMOC variability (Chafik et al. 2019) and water mass transformation (Chafik and Rossby 2019). Further, the Overturning in the Subpolar North Atlantic Programme (OSNAP) array, consisting of moorings from Labrador to the tip of Greenland (OSNAP West), and from the tip of Greenland to Scotland (OSNAP East), makes it possible to separate the impact of deep-water formation in the Labrador Sea, Iceland–Scotland region, and Nordic seas (Lozier et al. 2017). Based on the first 21 months of observations, Lozier et al. (2019) find that the AMOC variability is driven by water mass transformation north of the OSNAP East line (i.e., in the Iceland–Scotland region, Nordic seas, and farther north).

According to Heuzé et al. (2013), CMIP5 models overestimate deep-water formation resulting from open-water convection in the Southern Ocean at the expense of shelf processes not resolved by the models. In the North Atlantic, the simulated

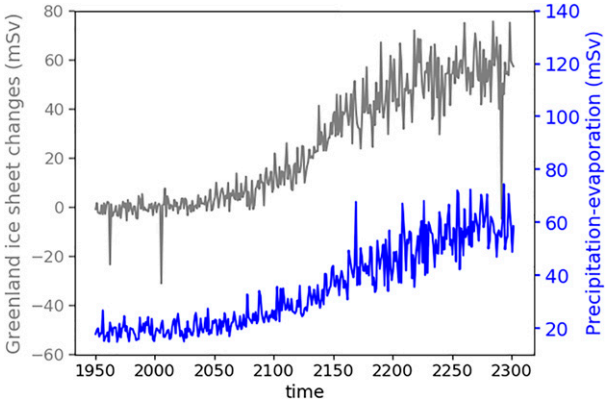

FIG. A1. Time series of the freshwater resulting from the Greenland ice sheet melting (gray line) and the rainfall (precipitation − evaporation) over the Arctic Basins and Nordic seas (blue line) in EC-Earth-PISM. The reduction in Greenland ice volume from around 2100 (Fig. 2) results in an increase in freshwater flux to the ocean. This freshwater flux is comparable to the rainfall over the Arctic Basins and Nordic seas from around 2200 (40 mSv) and stabilizes close to 60 mSv. However, part of the Greenland meltwater is transported southward (not studied here).

dense water produces a reasonable AMOC strength at 26°N, although the amount of open convection is unrealistically high in the models (Heuzé 2017). In fact, the cascading of dense shelf water off continental shelves has been described as one of the main mechanisms generating Arctic deep water (Aagaard et al. 1985). If dense shelf water were to be represented, we would expect the dynamics of the ArMOC, and its simulated strength over the next century, to be altered. In particular, the Arctic summer sea ice retreat and enhanced seasonality could lead to a strengthened ArMOC, as suggested by Bitz et al. (2006). In this hypothesis, the asymmetry between summer and winter sea ice reduction results in more winter sea ice formation and more brine rejection, enhancing dense-water formation on the shelves. On the other hand, reducing the importance of open water convection could imply a smaller impact of the northward shift of Arctic sea ice on the ArMOC.

5. Conclusions

The two simulations analyzed in this study show that accelerated melt of the Greenland ice sheet occurs after the simulated abrupt reduction in Arctic sea ice. This suggests that the additional freshwater input to the ocean, originating from the coupling with the Greenland ice sheet (PISM), does not significantly slow down the sea ice reduction in the EC-Earth-PISM model. The meltwater flux from Greenland exceeds 30 mSv by 2150, when the Arctic Ocean is nearly ice free, and reaches its mean maximal value of 53 mSv by 2200. At this point, the Greenland melt contributes by freshening and stabilizing the Arctic Basins, thereby promoting the weakening the Arctic meridional overturning circulation (ArMOC) north of the Greenland–Scotland ridge.

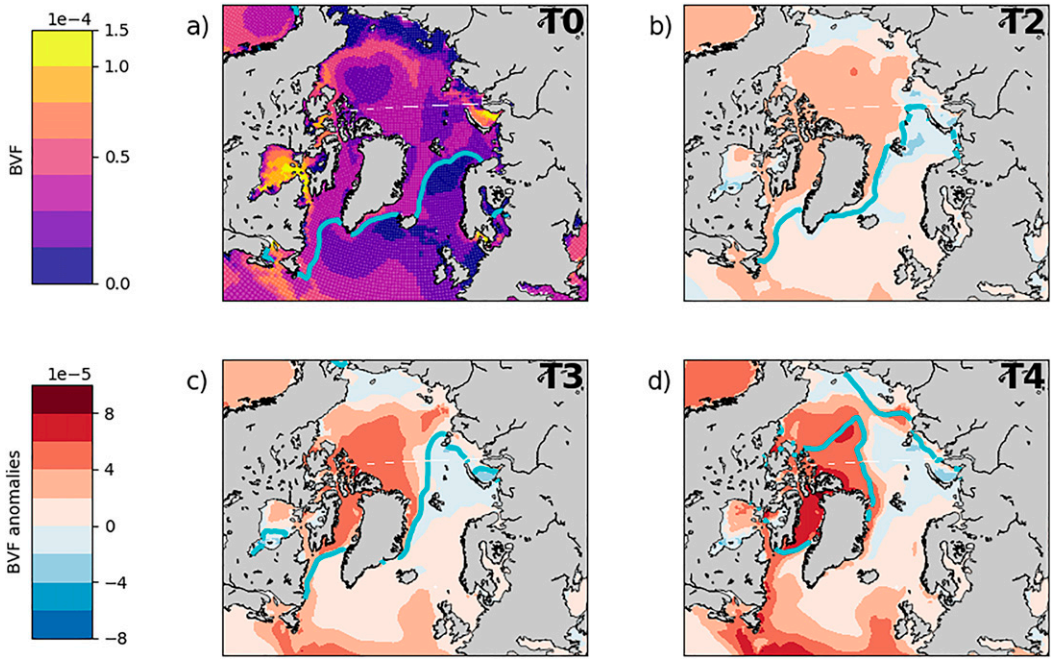

FIG. A2. Yearly mean Brunt–Väisälä frequencies in the top 800 m for the period (a) T0: 1970–80 in the EC-Earth-PISM simulation and anomalies during (b) T2: 2050–60, (c) T3: 2090–2100, and (d) T4: 2130–40 with respect to T0. The winter sea ice edge is plotted with the blue contour line. The blue color at the edge of the winter sea ice (Barents Sea and Nansen Basin) shows a weakening of the stratification while the rest of the ocean, and in particular the Arctic Basins and Nansen Basin excluded, becomes more stable.

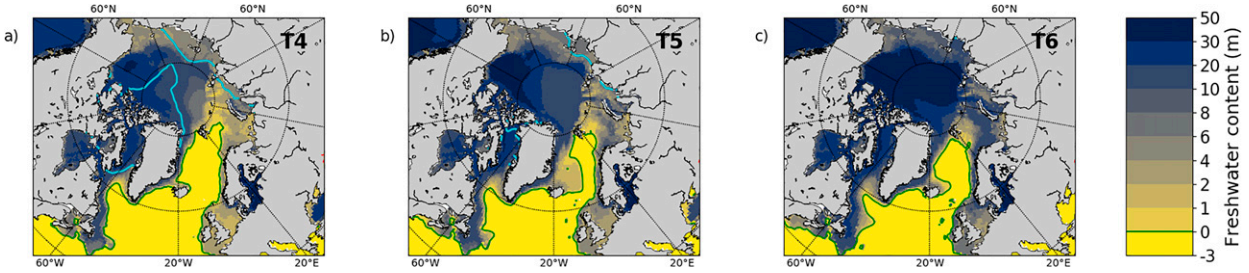

FIG. A3. Freshwater content as in Fig. 12, but during (a) T4: 2130–40, (b) T5: 2170–80, and (c) T6: 2290–2300. After T4, the Arctic Basins get consistently fresher, which can be linked to the water cycle acceleration and the ArMOC weakening that brings less saline Atlantic water to the Arctic.

Our key findings, related to the Arctic meridional overturning circulation (ArMOC), a new metric introduced to study the overturning changes north of the Greenland–Scotland ridge and into the central Arctic, are as follows:

- As the winter sea ice edge retreats into the interior Arctic Ocean from 1970 (Fig. 13a) to 2100 (Fig. 13b), the deep-water sites migrate north, enhancing the ArMOC.
- The simulated ArMOC strengthening contributes to a slowdown of the AMOC weakening at 26°N by 0.01 Sv yr^{-1} until 2100.
- After 2100, as the Arctic interior becomes ice free, there is a decoupling between the winter sea ice edge and deep-water formation. The upper ocean is strongly stratified due to large freshwater fluxes. Deep convection weakens in all basins, and the ArMOC is reduced, becoming negligible by 2200.
- In contrast to the ArMOC, the AMOC at 26°N is steadily reduced from 2000 to 2200. Hence, the AMOC and ArMOC appear decoupled in a warming climate, which warrants the need to study them separately.

Acknowledgments. The research leading to these results is part of the ice2ice project funded by the European Research Council under the European Community Seventh Framework Programme (FP7/2007-2013)/ERC Grant Agreement 610055. The research was supported by the Centre for Climate Dynamics at the Bjerknes Centre for Climate Research and the Trond Mohn Foundation under Grant Agreement BFS2016REK01 (A.B.).

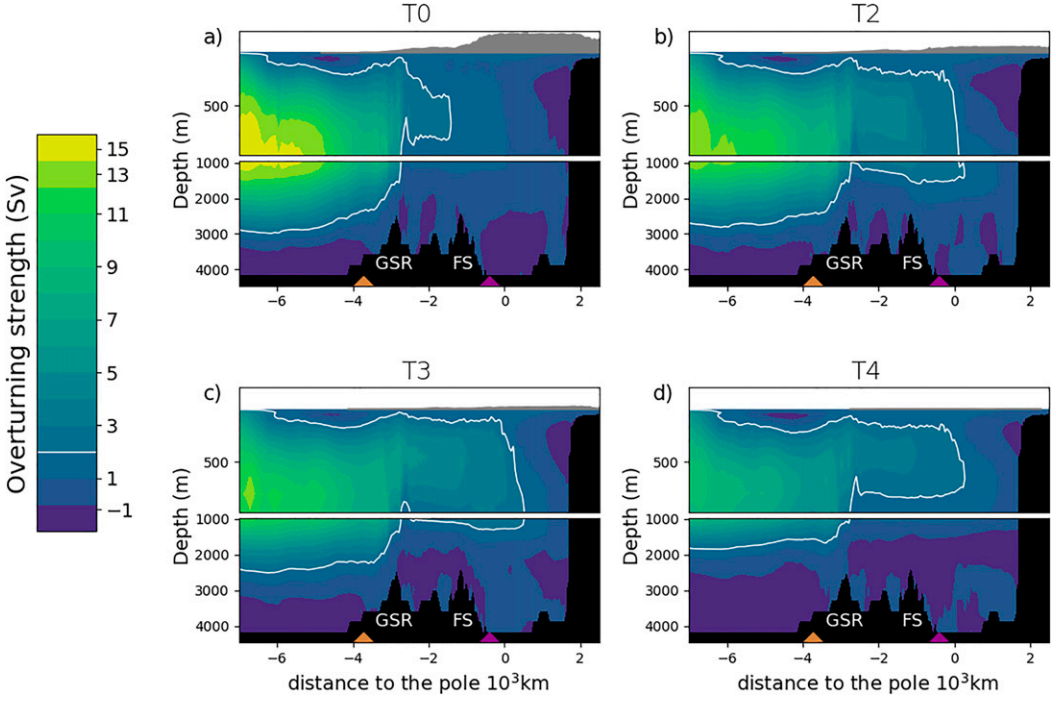

FIG. A4. ArMOC during (a) T0: 1970–80, (b) T2: 2050–60, (c) T3: 2090–2100, and (d) T4: 2130–40 in the EC-Earth-PISM simulation. As in Fig. 7, the white contour lines highlight the 2-Sv streamline and shows nicely the development of the ArMOC: its expansion from T0 to T3 and its reduction after T3.

We are grateful to Julian Mak for adapting functions of the CDFTOOLS program, in particular, cdfmocsig, into Python and sharing them on GitHub (https://github.com/julianmak/NEMO-related?files=1; personal website: https://nemo-related.readthedocs.io/en/latest/). Finally, we wish to thank Ida Margrethe Ringgaard for her help with the model outputs, Helene Asbjørnsen for her friendly review, and three anonymous reviewers for good suggestions that improved the manuscript.

Data availability statement. The Argo mixed layer database used in this study is available online at http://mixedlayer.ucsd.edu (see also Holte et al. 2017). The hydrographic dataset from Huang et al. (2020) consists of observations from several archives that can be accessed as listed in their Supplementary Table 1. The combined hydrographic dataset is available on request from A.B. (Ailin.Brakstad@uib.no).

APPENDIX

Complementary Figures

Figure A1 is a complement to Fig. 2: the ice volume change of Greenland is converted into freshwater fluxes and compared to the increase in rainfall over the Arctic region. Figure A2 shows the stability of the top 500 m of the water column as a complement to the freshwater content displayed in Fig. 12. Figure A3 shows that the Arctic Basins and Barents and Kara Seas only get fresher after T4, which is consistent with the ArMOC weakening in Fig. 11. Finally, Fig. A4 intends to better show the ArMOC spatial extension in time, as a complement to Fig. 8. . . .

REFERENCES

Aagaard, K., and E. C. Carmack, 1989: The role of sea ice and other fresh water in the Arctic circulation. *J. Geophys. Res.*, **94**, 14485, https://doi.org/10.1029/JC094iC10p14485.

——, J. H. Swift, and E. C. Carmack, 1985: Thermohaline circulation in the Arctic Mediterranean Seas. *J. Geophys. Res.*, **90**, 4833, https://doi.org/10.1029/JC090iC03p04833.

Athanase, M., C. Provost, M. D. Pérez-Hernández, N. Sennéchael, C. Bertosio, C. Artana, G. Garric, and J.-M. Lellouche, 2020: Atlantic water modification north of Svalbard in the Mercator physical system from 2007 to 2020. *J. Geophys. Res. Oceans*, **125**, e2020JC016463, https://doi.org/10.1029/2020JC016463.

Belonenko, T. V., A. M. Fedorov, I. L. Bashmachnikov, and V. R. Foux, 2018: Current intensity trends in the Labrador and Irminger Seas based on satellite altimetry data. *Izv. Atmos. Ocean. Phys.*, **54**, 1031–1038, https://doi.org/10.1134/S0001433818090074.

Bitz, C. M., P. R. Gent, R. A. Woodgate, M. M. Holland, and R. Lindsay, 2006: The influence of sea ice on ocean heat uptake in response to increasing CO_2. *J. Climate*, **19**, 2437–2450, https://doi.org/10.1175/JCLI3756.1.

Böning, C. W., E. Behrens, A. Biastoch, K. Getzlaff, and J. L. Bamber, 2016: Emerging impact of Greenland meltwater on deepwater formation in the North Atlantic Ocean. *Nat. Geosci.*, **9**, 523–527, https://doi.org/10.1038/ngeo2740.

Brakstad, A., K. Våge, L. Håvik, and G. W. K. Moore, 2019: Water mass transformation in the Greenland Sea during the period 1986–2016. *J. Phys. Oceanogr.*, **49**, 121–140, https://doi.org/10.1175/JPO-D-17-0273.1.

Brodeau, L., and T. Koenigk, 2016: Extinction of the northern oceanic deep convection in an ensemble of climate model simulations of the 20th and 21st centuries. *Climate Dyn.*, **46**, 2863–2882, https://doi.org/10.1007/s00382-015-2736-5.

Broecker, W., G. Bond, M. Klas, E. Clark, and J. McManus, 1992: Origin of the northern Atlantic's Heinrich events. *Climate Dyn.*, **6**, 265–273, https://doi.org/10.1007/BF00193540.

Bueler, E., and J. Brown, 2009: Shallow shelf approximation as a "sliding law" in a thermomechanically coupled ice sheet model. *J. Geophys. Res.*, **114**, F03008, https://doi.org/10.1029/2008JF001179.

Chafik, L., and T. Rossby, 2019: Volume, heat, and freshwater divergences in the subpolar North Atlantic suggest the Nordic Seas as key to the state of the meridional overturning circulation. *Geophys. Res. Lett.*, **46**, 4799–4808, https://doi.org/10.1029/2019GL082110.

——, J. E. Øie Nilsen, S. Dangendorf, G. Reverdin, and T. Frederikse, 2019: North Atlantic Ocean circulation and decadal sea level change during the altimetry era. *Sci. Rep.*, **9**, 1041, https://doi.org/10.1038/s41598-018-37603-6.

Cheng, W., J. C. Chiang, and D. Zhang, 2013: Atlantic meridional overturning circulation (AMOC) in CMIP5 models: RCP and historical simulations. *J. Climate*, **26**, 7187–7197, https://doi.org/10.1175/JCLI-D-12-00496.1.

Cunningham, S., 2008: Monitoring the Atlantic meridional overturning circulation at 26.5°N: Rapid-watch. National Oceanography Centre Southampton Research and Consultancy Rep. 59, 18 pp., http://nora.nerc.ac.uk/id/eprint/165106/1/NOCS_R%26C_59.pdf.

Davis, P. E., C. Lique, H. L. Johnson, and J. D. Guthrie, 2016: Competing effects of elevated vertical mixing and increased freshwater input on the stratification and sea ice cover in a changing Arctic Ocean. *J. Phys. Oceanogr.*, **46**, 1531–1553, https://doi.org/10.1175/JPO-D-15-0174.1.

de Boyer Montégut, C., G. Madec, A. S. Fischer, A. Lazar, and D. Iudicone, 2004: Mixed layer depth over the global ocean: An examination of profile data and a profile-based climatology. *J. Geophys. Res.*, **109**, C12003, https://doi.org/10.1029/2004JC002378.

de Jong, M. F., and L. de Steur, 2016: Strong winter cooling over the Irminger Sea in winter 2014–2015, exceptional deep convection, and the emergence of anomalously low SST. *Geophys. Res. Lett.*, **43**, 7106–7113, https://doi.org/10.1002/2016GL069596.

Fairbanks, R. G., 1990: The age and origin of the "Younger Dryas climate event" in Greenland ice cores. *Paleoceanography*, **5**, 937–948, https://doi.org/10.1029/PA005i006p00937.

Fichefet, T., and M. A. M. Maqueda, 1997: Sensitivity of a global sea ice model to the treatment of ice thermodynamics and dynamics. *J. Geophys. Res.*, **102**, 12 609–12 646, https://doi.org/10.1029/97JC00480.

——, C. Poncin, H. Goosse, P. Huybrechts, I. Janssens, and H. L. Treut, 2003: Implications of changes in freshwater flux from the Greenland ice sheet for the climate of the 21st century. *Geophys. Res. Lett.*, **30**, 1911, https://doi.org/10.1029/2003GL017826.

Hazeleger, W., and Coauthors, 2012: EC-Earth V2.2: Description and validation of a new seamless earth system prediction model. *Climate Dyn.*, **39**, 2611–2629, https://doi.org/10.1007/s00382-011-1228-5.

Heuzé, C., 2017: North Atlantic deep water formation and AMOC in CMIP5 models. *Ocean Sci.*, **13**, 609–622, https://doi.org/10.5194/os-13-609-2017.

——, K. J. Heywood, D. P. Stevens, and J. K. Ridley, 2013: Southern Ocean bottom water characteristics in CMIP5 models. *Geophys. Res. Lett.*, **40**, 1409–1414, https://doi.org/10.1002/grl.50287.

Hillaire-Marcel, C., A. D. Vernal, G. Bilodeau, and A. J. Weaver, 2001: Absence of deep-water formation in the Labrador Sea during the last interglacial period. *Nature*, **410**, 1073–1077, https://doi.org/10.1038/35074059.

Holte, J., L. D. Talley, J. Gilson, and D. Roemmich, 2017: An Argo mixed layer climatology and database. *Geophys. Res. Lett.*, **44**, 5618–5626, https://doi.org/10.1002/2017GL073426.

Huang, J., R. S. Pickart, R. X. Huang, P. Lin, A. Brakstad, and F. Xu, 2020: Sources and upstream pathways of the densest overflow water in the Nordic Seas. *Nat. Commun.*, **11**, 5389, https://doi.org/10.1038/s41467-020-19050-y.

Jahn, A., and M. M. Holland, 2013: Implications of Arctic sea ice changes for North Atlantic deep convection and the meridional overturning circulation in CCSM4-CMIP5 simulations. *Geophys. Res. Lett.*, **40**, 1206–1211, https://doi.org/10.1002/grl.50183.

Kim, W. M., S. Yeager, and G. Danabasoglu, 2020: Revisiting the causal connection between the great salinity anomaly of the 1970s and the shutdown of Labrador Sea deep convection. *J. Climate*, **34**, 675–696, https://doi.org/10.1175/JCLI-D-20-0327.1.

Koenigk, T., L. Brodeau, R. G. Graversen, J. Karlsson, G. Svensson, M. Tjernström, U. Willén, and K. Wyser, 2013: Arctic climate change in 21st century CMIP5 simulations with EC-Earth. *Climate Dyn.*, **40**, 2719–2743, https://doi.org/10.1007/s00382-012-1505-y.

Kuhlbrodt, T., A. Griesel, M. Montoya, A. Levermann, M. Hofmann, and S. Rahmstorf, 2007: On the driving processes of the Atlantic meridional overturning circulation. *Rev. Geophys.*, **45**, RG2001, https://doi.org/10.1029/2004RG000166.

Lique, C., and M. D. Thomas, 2018: Latitudinal shift of the Atlantic meridional overturning circulation source regions under a warming climate. *Nat. Climate Change*, **8**, 1013–1020, https://doi.org/10.1038/s41558-018-0316-5.

——, H. L. Johnson, and Y. Plancherel, 2018: Emergence of deep convection in the Arctic Ocean under a warming climate. *Climate Dyn.*, **50**, 3833–3847, https://doi.org/10.1007/s00382-017-3849-9.

Lozier, M. S., and Coauthors, 2017: Overturning in the subpolar North Atlantic program: A new international ocean observing system. *Bull. Amer. Meteor. Soc.*, **98**, 737–752, https://doi.org/10.1175/BAMS-D-16-0057.1.

——, and Coauthors, 2019: A sea change in our view of overturning in the subpolar North Atlantic. *Science*, **363**, 516–521, https://doi.org/10.1126/science.aau6592.

Madec, G., 2008: NEMO ocean engine. IPSL Note du Pôle de Modélisation 27, 209 pp.

McCarthy, G. D., and Coauthors, 2015: Measuring the Atlantic meridional overturning circulation at 26°N. *Prog. Oceanogr.*, **130**, 91–111, https://doi.org/10.1016/j.pocean.2014.10.006.

Nghiem, S. V., I. G. Rigor, D. K. Perovich, P. Clemente-Colón, J. W. Weatherly, and G. Neumann, 2007: Rapid reduction of Arctic perennial sea ice. *Geophys. Res. Lett.*, **34**, L19504, https://doi.org/10.1029/2007GL031138.

Notz, D., and J. Stroeve, 2016: Observed Arctic sea-ice loss directly follows anthropogenic CO_2 emission. *Science*, **354**, 747–750, https://doi.org/10.1126/science.aag2345.

——, and Coauthors, 2020: Arctic sea ice in CMIP6. *Geophys. Res. Lett.*, **47**, e2019GL086749, https://doi.org/10.1029/2019GL086749.

Nummelin, A., C. Li, and L. H. Smedsrud, 2015: Response of Arctic Ocean stratification to changing river runoff in a column model. *J. Geophys. Res. Oceans*, **120**, 2655–2675, https://doi.org/10.1002/2014JC010571.

Pérez-Hernández, M. D., and Coauthors, 2019: Structure, transport, and seasonality of the Atlantic water boundary current north of Svalbard: Results from a yearlong mooring array. *J. Geophys. Res. Oceans*, **124**, 1679–1698, https://doi.org/10.1029/2018JC014759.

Rawlins, M. A., and Coauthors, 2010: Analysis of the Arctic system for freshwater cycle intensification: Observations and expectations. *J. Climate*, **23**, 5715–5737, https://doi.org/10.1175/2010JCLI3421.1.

Smeed, D. A., and Coauthors, 2018: The North Atlantic Ocean is in a state of reduced overturning. *Geophys. Res. Lett.*, **45**, 1527–1533, https://doi.org/10.1002/2017GL076350.

Smith, R. S., and J. M. Gregory, 2009: A study of the sensitivity of ocean overturning circulation and climate to freshwater input in different regions of the North Atlantic. *Geophys. Res. Lett.*, **36**, L15701, https://doi.org/10.1029/2009GL038607.

Stroeve, J., and D. Notz, 2018: Changing state of Arctic sea ice across all seasons. *Environ. Res. Lett.*, **13**, 103001, https://doi.org/10.1088/1748-9326/aade56.

Taylor, K. E., R. J. Stouffer, and G. A. Meehl, 2012: An overview of CMIP5 and the experiment design. *Bull. Amer. Meteor. Soc.*, **93**, 485–498, https://doi.org/10.1175/BAMS-D-11-00094.1.

Våge, K., and Coauthors, 2009: Surprising return of deep convection to the subpolar North Atlantic Ocean in winter 2007–2008. *Nat. Geosci.*, **2**, 67–72, https://doi.org/10.1038/ngeo382.

Valcke, S., 2006: OASIS3 user guide. PRISM Project Tech. Rep. 3, 64 pp.

van Vuuren, D. P., and Coauthors, 2011: The representative concentration pathways: An overview. *Climatic Change*, **109**, 5–31, https://doi.org/10.1007/s10584-011-0148-z.

Wang, H., S. Legg, and R. Hallberg, 2018: The effect of Arctic freshwater pathways on North Atlantic convection and the Atlantic meridional overturning circulation. *J. Climate*, **31**, 5165–5188, https://doi.org/10.1175/JCLI-D-17-0629.1.

Winkelmann, R., M. A. Martin, M. Haseloff, T. Albrecht, E. Bueler, C. Khroulev, and A. Levermann, 2011: The Potsdam Parallel Ice Sheet Model (PISM-PIK)—Part 1: Model description. *Cryosphere*, **5**, 715–726, https://doi.org/10.5194/tc-5-715-2011.

Yang, Q., T. H. Dixon, P. G. Myers, J. Bonin, D. Chambers, and M. R. V. D. Broeke, 2016: Correction: Corrigendum: Recent increases in Arctic freshwater flux affects Labrador Sea convection and Atlantic overturning circulation. *Nat. Commun.*, **7**, 13545, https://doi.org/10.1038/ncomms13545.

Yashayaev, I., and J. W. Loder, 2017: Further intensification of deep convection in the Labrador Sea in 2016. *Geophys. Res. Lett.*, **44**, 1429–1438, https://doi.org/10.1002/2016GL071668.